Materials Advances

PAPER

View Article Online
View Journal | View Issue

Cite this: *Mater. Adv.*, 2025, **6**, 8713

The origin of annealing atmosphere-dependent defect formation and photocathodic behaviour in $BiFeO_3$ thin films

Syeda Reha Khadri, [a] N. V. Srihari, [b] K. K. Nagaraja [b] and Dharmapura H. K. Murthy *[a]

Bismuth ferrite ($BiFeO_3$) offers a unique blend of advantages—made of earth-abundant materials, capable of harnessing visible light ($\lambda \leq 600$ nm), and the prospect of piezocatalysis due to its inherent ferroelectric behaviour. Despite these advantages, the inadequate photocatalytic performance of $BiFeO_3$ is attributed to charge carrier recombination/trapping processes, promoted by defects formed upon varying the synthesis parameters. This work investigates the effect of the annealing atmosphere (argon or ambient air) on structural/optoelectronic properties and photoelectrochemical water splitting. Though optical absorption and the electrochemical surface area remained virtually similar, almost four times enhancement in photocathodic current density is observed for $BiFeO_3$ annealed in argon compared to that annealed in ambient air. This intriguing observation is rationalised based on the mutually correlated complex defect chemistry, Fermi level position, band bending profile, and efficiency of the interfacial charge transfer process. The interaction of Bi (due to its volatile nature) with its surrounding gas during the annealing process eventually determines the overall optoelectronic properties of $BiFeO_3$. Results offer a simple and facile yet effective strategy to engineer defects by just controlling the annealing atmosphere without doping or complicated post-synthesis processes. Discussed mechanistic insights shed light on the vulnerable nature of defects in $BiFeO_3$ and tuning them rationally for enhancing the solar fuel production.

Received 1st September 2025,
Accepted 13th October 2025

DOI: 10.1039/d5ma00995b

rsc.li/materials-advances

1. Introduction

Considering the ever-rising global energy demand and carbon emissions from fossil fuels, it is critical to utilise renewable energy sources. Harvesting abundantly available sunlight *via* the photocatalytic/photoelectrochemical (PEC) method to produce solar fuels offers a sustainable approach. However, to realise solar fuel production at scale, photocatalyst design plays a key role.[1] Among the several photocatalysts developed, metal oxides ($SrTiO_3$, TiO_2, *etc.*) are still extensively used, despite having a wide band gap capable of absorbing only ultraviolet light.[2–4] To further enhance the solar fuel production efficiency, it is essential for a photocatalyst to be earth-abundant and simultaneously absorb a wide part of the solar spectrum. For instance, visible light absorbing Bi-based photocatalysts such as $BiVO_4$, modified with a cocatalyst, have been utilized to effectively harness the photogenerated holes for PEC water splitting, achieving an incident photon-to-current efficiency (IPCE) of 34.37%.[5] In this context, bismuth ferrite ($BiFeO_3$ (BFO)), another Bi-based photocatalyst, is a promising visible-light ($\lambda \leq 600$ nm) absorbing photocatalyst. BFO is susceptible to doping at both Bi and Fe sites due to its perovskite-type structure,[6] thus offering tunable optoelectronic properties. In addition, the prospect of phase-dependent multiferroic behaviour is proposed to enhance charge separation yield; consequently, the efficiency of photocatalytic reaction in BFO is amenable.[7,8] Though other Bi-based photocatalysts, such as $BiVO_4$ and bismuth oxyhalides, are extensively investigated,[9–14] utilization of BFO for photocatalytic/PEC water splitting reaction remains unexplored, despite its promising prospects and advantages.

A few challenges limiting the effective utilization of BFO for PEC water splitting application are (i) difficulty in preparing phase-pure BFO, (ii) inherent challenges in controlling stoichiometry that lead to ubiquitous defects affecting charge carrier transport, (iii) lack of comprehensive correlation between synthesis conditions and the resulting optoelectronic properties, and (iv) pronounced charge carrier recombination

---

[a] *Department of Chemistry, Manipal Institute of Technology, Manipal Academy of Higher Education, Manipal, 576104, India. E-mail: murthy.dharmapura@manipal.edu*

[b] *Department of Physics, Manipal Institute of Technology, Manipal Academy of Higher Education, Manipal, 576104, India*

and trapping.[15,16] While these parameters collectively determine the PEC water splitting efficiency, their origin can be attributed to the unique properties of the elements in BFO and their electronic interaction. Among the constituents of BFO, Bi has a relatively lower melting point of ~271 °C. Hence, Bi is prone to escape from the lattice at an early stage during the synthesis of BFO, naturally resulting in the formation of Bi vacancies. Consequently, owing to the charge compensation mechanism, oxygen vacancies are mutually formed alongside Bi vacancies. This overall process leaves unpaired electrons that convert the valence state of Fe in BFO to Fe^{2+} from Fe^{3+} (expected as per ideal $BiFeO_{3.0}$ stoichiometry).[17] Collectively, the formation of Bi and oxygen defects influences the Fermi level (E_F) position, charge carrier transport, and electron–hole recombination.[18] Besides solar fuel production *via* PEC or photocatalytic approaches, BFO is a promising candidate for applications in piezoelectrics, ferroelectric materials, spintronics, sensors, and optoelectronics.[19,20] However, a major factor limiting the wider utilization of BFO is its inherently high leakage current correlated to oxygen vacancies.

A few approaches to control the vacancies include changing synthesis parameters and doping. Doping samarium at Bi sites of the BFO host enhanced the concentration of oxygen vacancies and consequently, PEC water splitting activity.[21,22] However, no consensus exists on how such vacancies promote (or hinder) electron–hole recombination and interfacial charge transfer processes, eventually affecting the PEC performance. Considering the role of the annealing atmosphere, BFO thin films annealed in an oxygen-rich atmosphere showed 3.5 times higher photoanodic current than BFO annealed in air.[23] Furthermore, BFO thin films annealed in oxygen showed lower crystallinity and a higher leakage current than samples annealed in air.[24] In contrast, another study revealed enhanced microstructural and electrical properties when annealed in oxygen.[25] Summarizing these observations, there is no agreement or mechanistic insight into how the annealing atmosphere controls Bi and/or oxygen vacancies that play a key role in the structural and optoelectronic properties of BFO. Hence, it is essential to establish comprehensive correlations between synthesis parameters and structural defects/vacancies to enhance the performance of BFO.

The key question we aim to address is how the annealing atmosphere impacts vacancy formation and reveals the underlying mechanism involved. In this direction, while keeping all other experimental parameters similar, only the heating atmosphere is systematically changed from ambient air to argon. The photocathodic current observed during the PEC reaction is correlated with structural/optoelectronic properties. Results highlight the role of the vulnerable and volatile nature of Bi atoms and their tendency to interact with the gas atmosphere in controlling the vacancies in BFO. Obtaining mechanistic insights into such often-ignored processes is key to enhancing PEC water-splitting performance and designing photocatalysts.

2. Experimental section

2.1. Synthesis of BFO thin films

BFO thin films were synthesised using bismuth(III) nitrate pentahydrate ($Bi(NO_3)_3 \cdot 5H_2O$; Merck), iron(III) nitrate nonahydrate ($Fe(NO_3)_3 \cdot 9H_2O$; Thermo Scientific), fluorine-doped tin oxide (FTO) substrates (Techinstro), acetic acid (Loba Chemie) and 2-methoxy ethanol (Isochem) as solvent. 0.3 M solution of $Bi(NO_3)_3 \cdot 5H_2O$ was prepared using acetic acid and 2-methoxy ethanol as solvents in a 1 : 3 ratio (10% excess Bi salt was added to compensate for Bi loss upon heating at higher temperatures). A 0.3 M solution of $Fe(NO_3)_3 \cdot 9H_2O$ in 2-methoxy ethanol was also prepared. The solutions were heated separately at 50 °C with constant stirring for 50 minutes. These two solutions were later mixed and heated at 50 °C for two hours under continuous stirring. The precursor solution was then spin-coated on the pretreated FTO substrates at 2000 rpm for 30 seconds and later dried at 150 °C for 10 minutes under ambient conditions. Subsequently, the samples were annealed in different atmospheres (argon or ambient air) at 500 °C for two hours in a furnace with an 8 °C ramp rate. For the ambient air-annealed sample, both ends of the tube furnace were kept open to allow circulation of ambient air. In the case of the argon-annealed sample, both ends of the tube furnace were closed, and a continuous argon flow was maintained at 150 sccm throughout the annealing process. The BFO thin films annealed in ambient air were labelled as "ambient air," while those annealed in a 100% argon atmosphere were labelled as "argon."

2.2. Structural, electrical and optoelectronic characterization tools

Grazing incidence X-ray diffraction (GI-XRD) was measured on a Rigaku SmartLab with a Cu Kα source of wavelength, λ = 1.54 Å. The GI-XRD pattern was recorded at 2θ values ranging from 20° to 80° with a step size of 0.02°. The ratio of Bi and Fe in each sample was determined through energy-dispersive X-ray spectroscopy (EDS) using an EVO MA 18 with an Oxford EDS (X-act). The reported ratio is the average composition recorded at three different sites of the thin films. The roughness parameter of the films was measured using an atomic force microscope (AFM) provided by Agilent Technologies.

X-ray photoelectron spectroscopy (XPS) and valence band XPS (VB-XPS) were employed to determine the valence state of the elements in the BFO thin films and the relative shift in the E_F. These measurements were conducted using a Thermo Scientific Kα X-ray photoelectron spectrometer. Spectral charge correction for the high-resolution XPS core level spectra was performed using the C1s peak at 284.8 eV. To further compare the oxygen vacancies in the two samples, leakage current was measured using a Radiant Precision Premier II Ferroelectric Tester. A voltage of 0.1 V was applied with 0.1 s soak time, followed by measuring the current for the next 0.1 s. Optical absorption of the synthesised thin films was measured using a UV-vis spectrophotometer from Thermo Fisher Scientific with an integrating sphere accessory using a step size of 1 nm. It includes the data of fraction of light absorbed (F_A) by the BFO thin films, calculated using the following equation (eqn (1)).

$$F_{\mathrm{A}} = 1 - \left(\frac{\%\,\mathrm{Transmittance}}{100} + \frac{\%\,\mathrm{Reflectance}}{100}\right) \quad (1)$$

2.3. Photoelectrochemical studies

PEC measurements were performed using a Metrohm Autolab PGSTAT 204 and a solar simulator from Holmarc (HR-SS300WRM1-100A) with an air mass (AM 1.5G) filter, and a 300 W xenon short arc lamp was used as the light source. A three-electrode system was used for the measurements, with platinum mesh and a reversible hydrogen electrode (RHE) being the counter and reference electrode, respectively. 0.1 M K_2SO_4 was used as the electrolyte (pH 5.6) for the PEC measurements. Cyclic voltammetry (CV) was performed for a potential range of 0 V to 1.2 V *vs.* RHE at a scan rate of 20 mV s^{-1}. Linear sweep voltammetry (LSV) was performed from 0.8 V to 0 V *vs.* RHE at a scan rate of 20 mV s^{-1} and 50 mV s^{-1}. The reported LSV and CV data include iR corrected potential values. The effect of light and the electron acceptor (H_2O_2) on the photocathodic current and stability of the BFO sample was studied using chronoamperometry measurements at −0.1 V *vs.* RHE for 2 hours and at 0 V *vs.* RHE for 30 minutes with dark and light intervals every alternate minute. The electrochemical surface area (ECSA) of both thin films was determined by recording CV in the non-faradaic region at scan rates ranging from 10 mV s^{-1} to 50 mV s^{-1}. The double layer capacitance (C_{dl}) was obtained from the plot of anodic current (j_a)–cathodic current (j_c) *vs.* the scan rate, at a given potential. The ECSA was then calculated using $C_{\mathrm{dl}}/C_{\mathrm{s}}$, where C_{s} is the specific capacitance of BFO. Electrochemical impedance spectroscopy (EIS) measurements were recorded at a DC potential of 0 V *vs.* RHE, across a frequency range of 5000 Hz to 0.1 Hz.

3. Results and discussion

The effect of the annealing atmosphere on the PEC performance of the BFO thin films will be discussed first, followed by offering optoelectronic and defect chemistry bases to rationalise the observations. The last part offers insight into enhancing the functions and diverse applications of BFO *via* defect engineering.

3.1. Effect of the annealing atmosphere on the PEC performance of BFO thin films

Fig. 1a compares the CV data of BFO thin films annealed in argon and ambient air. Both films show a significant enhancement in light-induced current in the cathodic side compared to the anodic side. This observation indicates a reduction reaction involving electrons and its potential application towards the hydrogen evolution reaction. Fig. 1b shows how the photocathodic current magnitude and onset potential values are sensitive to the annealing atmosphere. The BFO thin films annealed in ambient air and argon show a photocurrent density of −0.005 mA cm^{-2} and −0.019 mA cm^{-2} at 0 V *vs.* RHE, respectively. The four times increment in photocathodic current and a reduction in onset potential by 0.1 V suggest an ease in electron extraction for the BFO thin film annealed in argon compared to ambient air. Similar observations were noted in different batches of samples (with varying scan rates), demonstrating a consistent and unambiguous effect of the annealing atmosphere on the PEC performance (Fig. S1a).

To confirm the cathodic behaviour and prolonged stability, chronoamperometry measurements at 0 V and −0.1 V *vs.* RHE were performed. As depicted in Fig. 1c, the photocathodic current increased by an order of magnitude upon adding a small volume of electron acceptor (H_2O_2) to the electrolyte. This observation confirms that electrons are indeed the charge carriers involved in the reaction (Fig. S1b). Furthermore, consistent photocathodic behaviour for 2 hours under illumination (Fig. S2) and light response beyond 30 minutes of chronoamperometry measurements (Fig. 1c) confirm that the prepared BFO thin films are stable under operational conditions, therefore indicating that the annealing atmosphere does not affect the stability of BFO thin films. In the next section, we aim to understand how and why such enhancement in photocathodic behaviour is expected just by changing the annealing atmosphere.

3.2. Role of the annealing atmosphere in determining the PEC activity of BFO thin films

As discussed in Fig. 1, BFO films annealed in argon consistently demonstrated a higher photocathodic current and a lower onset potential compared to those annealed in ambient air. This difference in the photocathodic activity of BFO thin films upon merely changing the annealing atmosphere is quite intriguing. Typically, a higher PEC activity is primarily attributed to a greater ECSA of the photocatalyst.[26,27] The ECSA of argon annealed BFO thin films is 1.93 cm^2, while that of ambient air annealed BFO is 1.63 cm^2 (Fig. S1c and d). Although this suggests that argon-annealed BFO has relatively more active sites, this alone cannot explain the origin of four times enhancement in the photocathodic current of argon-annealed BFO thin films. In the next sections of the manuscript, we unravel the origin of such annealing-atmosphere-dependent PEC performance. To this end, we systematically investigate plausible reasons, such as the efficiency of (i) light absorption, (ii) charge carrier generation and transport, and (iii) interfacial charge transfer.[28]

To begin with, the effect of the annealing atmosphere on the magnitude of light absorbed is revealed by separately recording both transmittance and reflectance measurements using an integrating sphere. Fig. S3 compares the fraction of light absorbed, F_A (eqn (1)), for BFO thin films annealed in ambient air and argon. Both films show a similar absorption onset of ∼520 nm, in agreement with earlier reports.[30] However, noticing a minor difference of ∼0.02 in the F_A values between the samples is unlikely to explain the four times increment in the photocathodic current. Hence, enhanced PEC activity observed

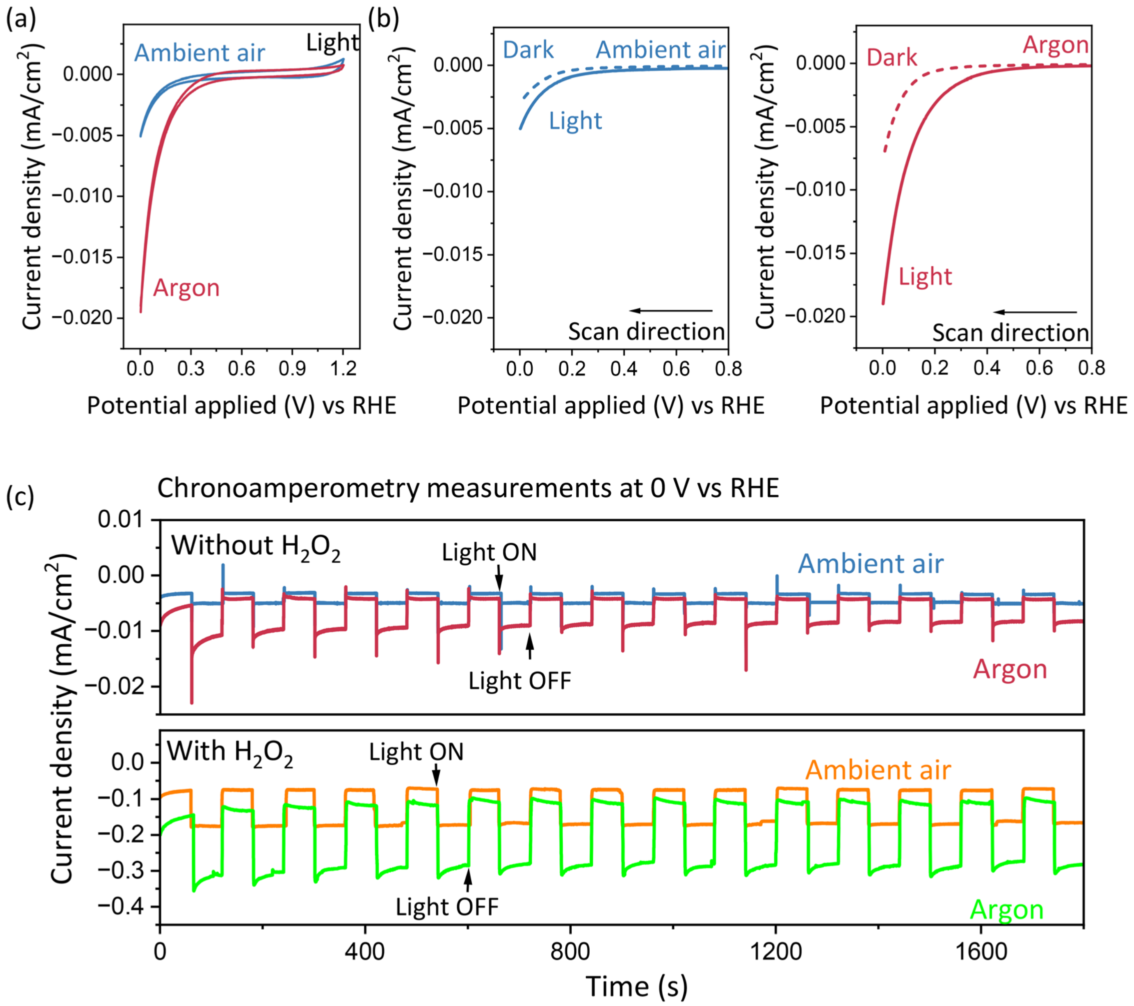

Fig. 1 (a) Comparison of CV data and photoinduced cathodic current density between BFO thin films annealed in ambient air and argon. (b) LSVs of BFO thin films annealed in ambient air and argon under dark and light conditions. Note that all CV and LSV data are corrected for iR. (c) Chronoamperometry data of BFO thin films annealed in ambient air and argon with 0.1 M K_2SO_4 as the electrolyte and in the presence of 0.3 mM H_2O_2 as an electron acceptor. Reaction conditions: AM 1.5 G; power density = 1000 W m^{-2}; pH = 5.6; scan rate = 20 mV s^{-1}.

for argon-annealed BFO cannot be attributed to an increase in the magnitude of light absorption.

Besides light absorption, the PEC performance is determined from the efficiency of the charge transfer process at the semiconductor/electrolyte interface. However, processes like charge carrier transport and recombination (both the bulk and the surface)[31] are governed by defects that are anticipated to be affected upon changing the annealing atmosphere. In this direction, the GI-XRD measurement is conducted to investigate changes in the structural properties between the films, which will offer insights into the defect formation.

Fig. 2a compares the GI-XRD patterns of BFO thin films annealed in argon and ambient air. The diffraction patterns and phase in both samples closely match the rhombohedral phase of BFO (ICSD 082614) and do not show secondary phases. Considering that a very thin layer of BFO is coated on FTO, peaks corresponding to the FTO substrate are also observed and are differentiated with an asterisk symbol. The peaks around 2θ values of 22.4°, 31.7°, and 32.0° are assigned to the (012), (104), and (110) planes, respectively. Among other diffraction patterns, the (012) plane of BFO is pronounced. Fig. 2b shows the (012) plane of BFO simulated using open-source software (Vesta) and how it is influenced by the presence of Bi atoms in the lattice. As depicted in Fig. 2c, a higher relative intensity of the (012) peak with respect to the (110) peak for BFO thin films annealed in argon compared to those annealed in ambient air is noticed. Such pronounced peak intensity indicates a higher amount of Bi in argon-annealed BFO; consequently, fewer Bi vacancies. The EDS analysis in Fig. 2d (and Fig. S4) indicates a higher Bi to Fe elemental ratio for BFO thin films annealed in argon (1.16) compared to those annealed in ambient air (0.77), further corroborating the conclusions from XRD analysis. The AFM analysis in Fig. S4c and d depicted a decrease in the average surface roughness from 8.5 nm to 6.2 nm upon changing the annealing atmosphere from ambient air to argon. This observation further hints a reduction in the surface defect concentration for BFO annealed in argon. Thus, the first significant difference upon changing

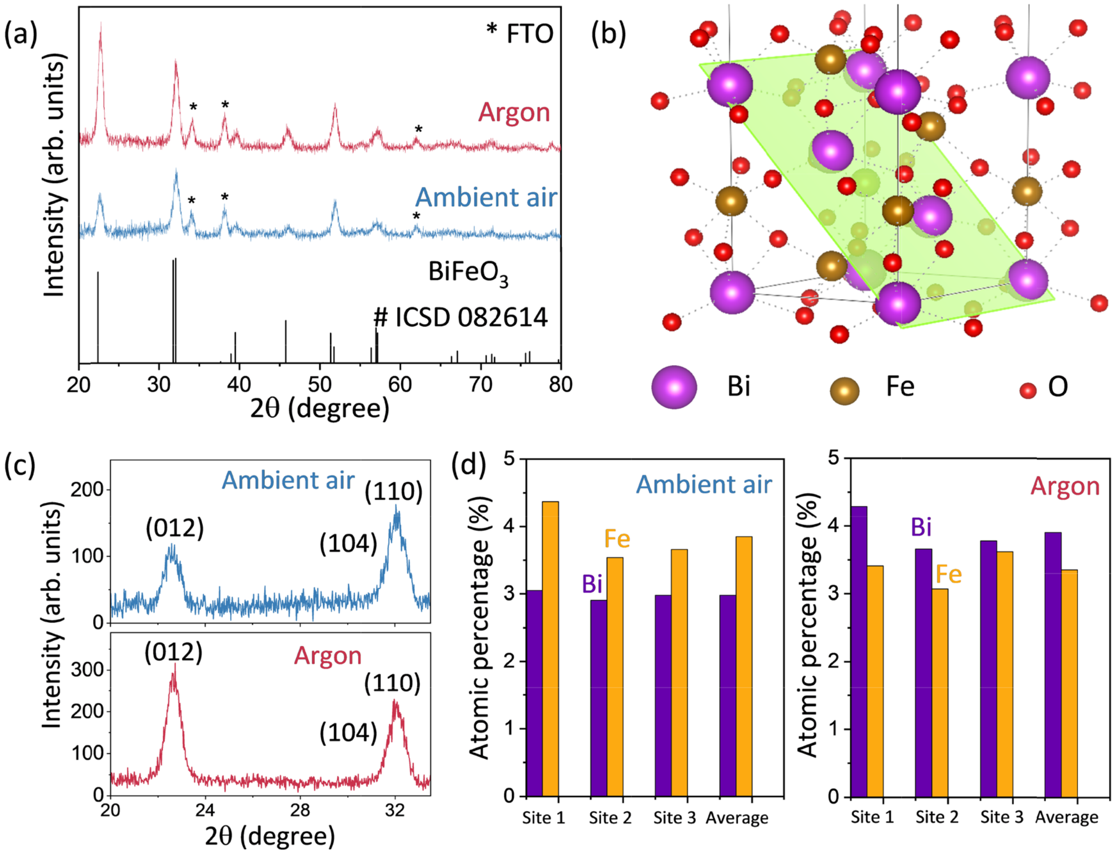

Fig. 2 (a) GI-XRD patterns of BFO thin films annealed in ambient air and argon. The asterisk corresponds to peaks from the FTO substrates.[29] (b) (012) plane of BFO, constituting Bi atoms, simulated using Vesta software as per the standard crystallography open database (**https://www.crystallography.net/cod/**). (c) Comparison of relative peak intensities corresponding to (012) and (110) planes for ambient air annealed and argon annealed BFO thin films. (d) The atomic percentages of Bi and Fe in BFO thin films annealed in ambient air and argon atmospheres deduced from EDS measurements at three different sites of the thin films.

the annealing atmosphere is in the vacancies. Specifically, the concentration of Bi vacancies is higher in BFO thin films annealed in ambient air compared to those annealed in argon.

Note that the XRD and EDS data discussed earlier represent the bulk properties of the BFO system. To obtain information on the vacancies formed and their influence on the constituent elements of BFO upon changing the annealing atmosphere, surface-sensitive high-resolution XPS analysis measurements are conducted.

The survey spectra in Fig. S5 confirm the presence of Bi, Fe, and O in the BFO thin films. Fig. 3a presents the high-resolution XPS core spectra of Bi 4f, which are deconvoluted into four peaks. Two prominent peaks around 158.6 eV and 163.9 eV, with a spin–orbit coupling energy of ∼5.31 eV, correspond to the Bi^{3+} state.[32] Two other peaks at lower binding energies are assigned to $Bi^{(3-x)+}$, associated with oxygen vacancies.[10] Table S1 details Bi 4f binding energy values and the area under the peak for both films. Since the Bi^{3+} peak corresponds to the Bi in the perovskite lattice, an increase in its area confirms a greater amount of Bi (fewer Bi vacancies) in BFO thin films annealed in argon compared to those annealed in ambient air.

Due to the variations in Bi vacancies, a mutually correlated change in oxygen vacancies is anticipated. Fig. 3b presents the XPS spectra of O 1s, which are deconvoluted into three peaks. The O_i peak (∼529.3 eV) corresponds to the metal–oxygen bonds in the BFO lattice. In contrast, the peaks O_{ii} and O_{iii} are assigned to the dangling bonds and the surface-adsorbed oxygen, respectively.[33] The contribution from each deconvoluted peak helps to estimate the oxygen vacancies in the synthesised thin films. According to the data in Table S2 deduced by rigorous fitting of the XPS data, the O_i peak of ambient air annealed BFO accounts for 41%, while the peaks associated with oxygen vacancies (O_{ii} + O_{iii}) account for 59%. Annealing BFO thin films in argon increases the O_i peak contribution, corresponding to the perovskite oxygen, to 67.6%, decreasing the oxygen vacancies to 32.4%.

Pronounced formation of oxygen vacancies can further be validated by determining the valence state of Fe in BFO.[34] Though the theoretical oxidation state of iron in BFO is Fe^{3+}, the occurrence of Fe^{2+} due to the formation of oxygen vacancies is often observed. A higher ratio of Fe^{2+} to Fe^{3+} ions indicates the presence of more oxygen vacancies. The peaks in the XPS core spectra of Fe 2p in Fig. 3c are split into a doublet of Fe $2p_{3/}$

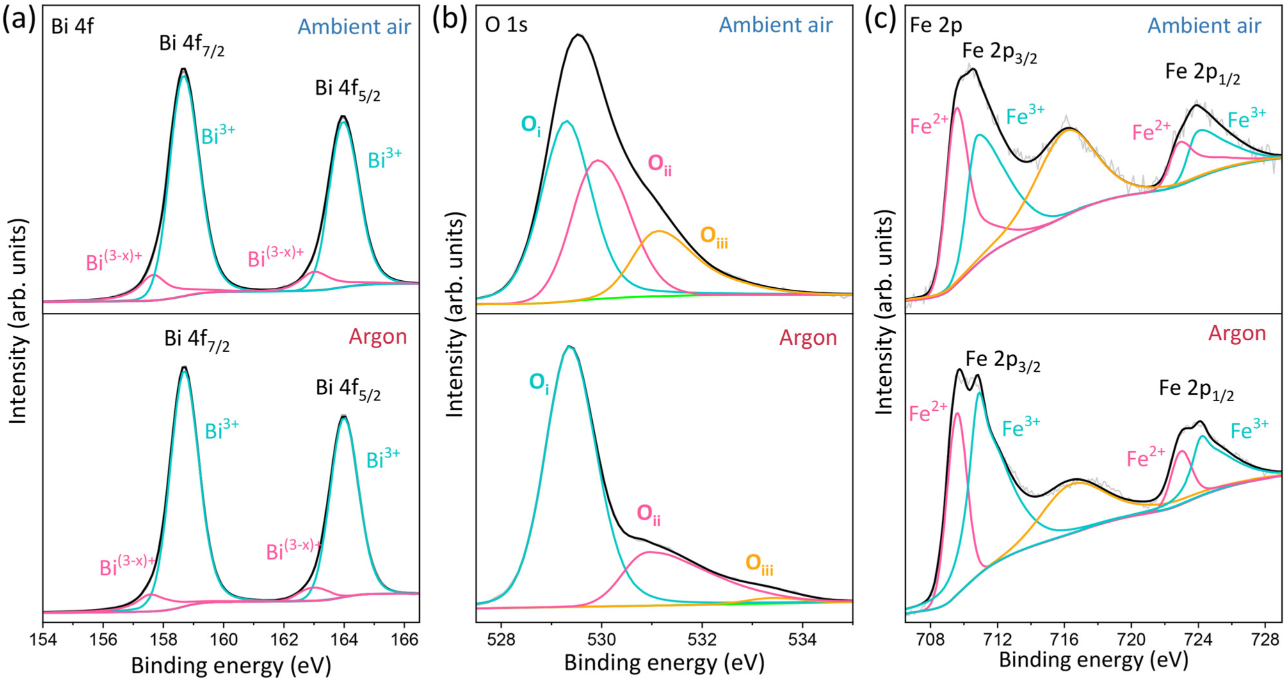

Fig. 3 XPS core level spectra of BFO thin films annealed in ambient air and argon: (a) Bi 4f region, (b) O 1s region and (c) Fe 2p region.

$_2$ and Fe $2p_{1/2}$, further deconvoluted into two peaks. The peaks at lower binding energies of ∼709.5 eV and ∼722.9 eV are assigned to the Fe^{2+} state, while the peaks around 710.8 eV and 724.0 eV correspond to the Fe^{3+} state. The peak at ∼716 eV is a satellite peak. Table S3 reports the Fe^{3+}/Fe^{2+} ratio of BFO thin films annealed in different atmospheres. The lower percentage of Fe^{3+} in ambient air annealed BFO implies greater fluctuation of the valence state of Fe due to relatively more oxygen vacancies.[17,35]

XPS analysis (summarized in Table 1) revealed a reduction in the concentrations of Bi and mutually correlated oxygen vacancies for BFO thin films annealed in argon compared to those annealed in ambient air. To further corroborate these observations, the leakage current that is directly controlled by the oxygen vacancy concentration[36] in BFO thin films was measured. As expected, BFO thin films annealed in argon demonstrated lower leakage current compared to those annealed in ambient air (Fig. S6). This observation shows the profound effect of the annealing atmosphere on the vacancies and the resulting defects at both macroscopic (leakage current) and surface (XPS) levels. At the same time, these data show an alternate avenue to reduce leakage current just by changing the annealing atmosphere, unlike the usually employed elemental doping. Decreasing the leakage current by using a facile and simple approach aids in wider application of BFO in piezoelectrics, sensors, actuators, and other optoelectronic devices.

Table 2 presents a comprehensive summary of all the data and observations discussed earlier. However, the origin of the annealing atmosphere determining the defects and eventually the PEC performance needs to be elucidated. This question will be addressed in subsequent sections.

3.3. Mechanistic insight into the annealing-atmosphere-dependent defect formation and PEC performance

To understand the mechanism, it is essential to get an insight into the possible interactions of BFO constituent elements with the annealing atmosphere. Due to the affinity of oxygen (in ambient air) with Bi,[37] a pronounced interaction between Bi and atmospheric oxygen is anticipated. As a result, the escape of Bi during the lattice formation is favoured while annealing BFO thin films in ambient air. This notion agrees with earlier work demonstrating a strong correlation between the Bi defect

Table 1 A summary of changes in the valence states of the constituent elements of BFO deduced from XPS analysis

Constituent elements of BFO	Annealed in argon	Annealed in ambient air
Bi 4f	Bi^{3+} (91.24%), and $Bi^{(3-x)+}$ (8.76%, resulting due to oxygen vacancies)	Bi^{3+} (86.32%) and $Bi^{(3-x)+}$ (13.68%, resulting due to oxygen vacancies)
Fe 2p	Fe^{3+} (71.73%) and Fe^{2+} (28.27%, formed due to oxygen vacancies)	Fe^{3+} (55.67%) and Fe^{2+} (44.32%, formed due to oxygen vacancies)
O 1s	O^{2-} corresponding to the perovskite lattice (67.6%)	O^{2-} corresponding to the perovskite lattice (41%)

Table 2 A summary of observations on BFO thin films annealed in ambient air and argon

Properties	Comparison
Photocathodic current density	Ambient air annealed BFO < argon annealed BFO
Optical absorption	Ambient air annealed BFO ≈ argon annealed BFO
Bi vacancies	Ambient air annealed BFO > argon annealed BFO
Oxygen vacancies	Ambient air annealed BFO > argon annealed BFO
Leakage current density	Ambient air annealed BFO > argon annealed BFO

formation energy and the partial pressure of oxygen employed during the annealing process.[38,39] The escape of Bi from the lattice accelerates the formation of Bi vacancies in ambient air annealed BFO. To compensate for the charge imbalance induced by Bi vacancies, more oxygen vacancies are to be formed, as presented in eqn (2). As a result, the unpaired electrons generated due to oxygen vacancy formation will subsequently reduce the valence state of Fe from Fe^{3+} to Fe^{2+}, as shown in eqn (3). These processes collectively induce a higher concentration of Bi vacancies, oxygen vacancies, and Fe^{2+} in BFO thin films annealed in ambient air.

$$\mathrm{BiFeO_3} \rightarrow \mathrm{Bi}_{1-x}\mathrm{FeO}_{3-3x} + x\mathrm{V}_{\mathrm{Bi}} + 3x\mathrm{V}_{\mathrm{O}} + \frac{3x}{2}\mathrm{O_2} + 3\mathrm{e}^- \quad (2)$$

$$\mathrm{BiFeO_3} \rightarrow \mathrm{Bi}_{1-x}\mathrm{Fe(III)}_{1-x}\mathrm{Fe(II)}_{x}\mathrm{O}_{3-3x} + x\mathrm{V}_{\mathrm{Bi}} + 3x\mathrm{V}_{\mathrm{O}} + \frac{3x}{2}\mathrm{O_2} + 2\mathrm{e}^- \quad (3)$$

In contrast, when BFO thin films are annealed in an argon atmosphere (oxygen-free), the interaction between atmospheric oxygen and Bi is virtually absent. Hence, escape of volatile Bi atoms from the lattice is not favoured. As a result, fewer Bi vacancies are formed, leading to a relative decrease in oxygen vacancies. Under argon annealing, oxygen vacancy formation is induced by the absence of oxygen in the annealing atmosphere, but it is unlikely due to the charge compensation mechanism. Fig. 4 illustrates variations in the vacancy formation mechanism upon changing the annealing atmosphere from ambient air to argon.

According to XRD and XPS results and all collective discussions earlier, the annealing atmosphere controls vacancies and their concentration in BFO. However, how they impact PEC performance is unclear. In this direction, the effect of such vacancies on the optoelectronic properties will be investigated. The types of defects and their concentration dictate the E_F of

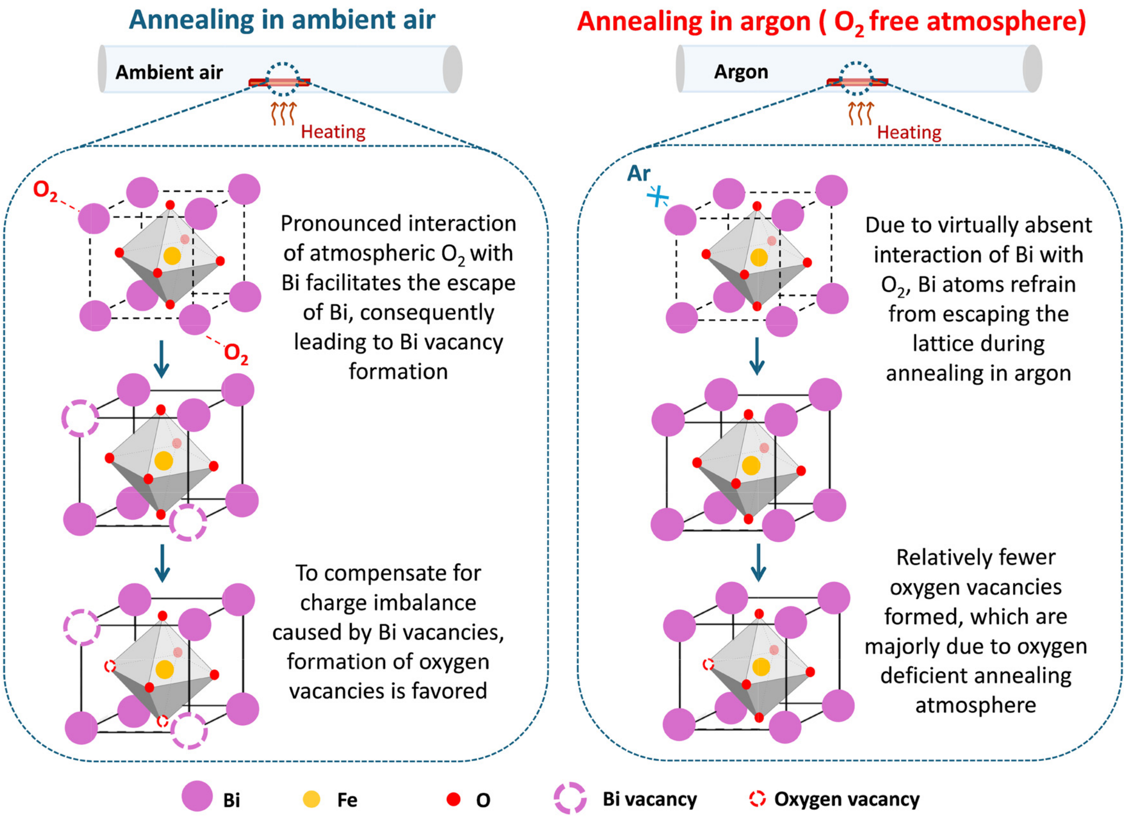

Fig. 4 Illustrating variations in the interactions between constituents of BFO thin films with the annealing atmosphere (argon or ambient air) and the resulting defect chemistry.

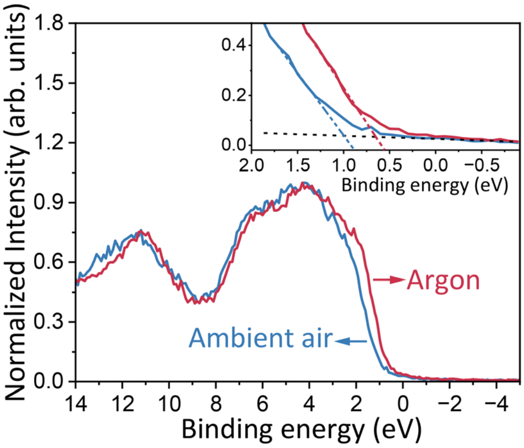

Fig. 5 VB-XPS spectra of BFO thin films annealed in ambient air and argon. The inset is zoomed in to understand the onset.

BFO. In $BaTiO_3$, another type of perovskite oxide, reducing the concentration of Ti^{3+} and mutually correlated oxygen vacancies rendered a p-type behaviour from its well-known n-type nature.[40] In the case of BFO, annealing atmosphere-dependent changes in the concentration of Bi and oxygen vacancies are expected to strongly influence the carrier density. Fig. 5 compares the VB-XPS data between BFO thin films. Considering the relative shift and differences in the higher (or lower) binding energy, annealing atmosphere dependent changes in the E_F can be deduced. Noticing the VB onset closer to the VB indicates the p-type characteristics of synthesised BFO thin films, further validating the photocathodic behaviour discussed in Fig. 1. BFO thin films annealed in argon showed a shift of ∼0.3 eV towards a lower binding energy compared to those annealed in ambient air. This observation indicates a pronounced p-type behaviour of argon-annealed BFO thin films attributed to a decrease in the concentration of oxygen vacancies, in good agreement with noticing a lower leakage current (Fig. S6) discussed earlier.

Next, to understand how such changes in the E_F position impact the PEC performance, the band bending model and its plausible role in promoting the charge transfer process are invoked. The E_F positions for both ambient air and argon annealed BFO thin films are obtained from VB-XPS. When BFO thin films encounter the electrolyte interface, the E_F of the BFO thin film and electrolyte[41] aligns to establish an electrostatic equilibrium. Consequently, a space-charge region is formed, resulting in downward band bending, as illustrated in Fig. 6. Upon illumination, the photogenerated electrons in the conduction band of BFO move towards the interface by virtue of the electric field gradient established upon equilibration, thus favouring the reduction reaction.[42]

In the case of the argon annealed sample, owing to the relative shift of E_F towards the valence band, the steepness of band bending is increased compared to ambient air annealed BFO. As a result, the formation of a pronounced electric field gradient in argon annealed BFO favours electron transfer towards the surface and reduces the possibility of electron–

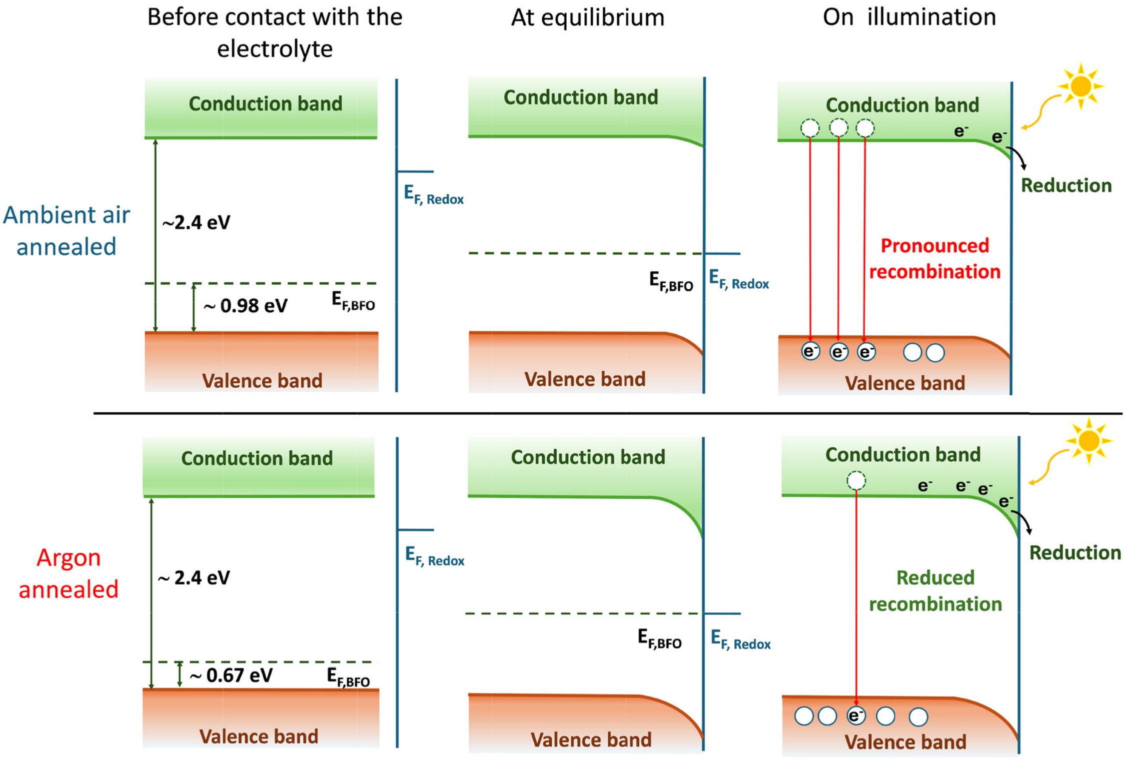

Fig. 6 Simplified illustration of the proposed band bending mechanism in ambient air and argon annealed BFO thin films. $E_{F,Redox}$ refers to the Fermi energy level of the electrolyte corresponding to the reduction reaction and $E_{F,BFO}$ denotes the Fermi energy level position of BFO.

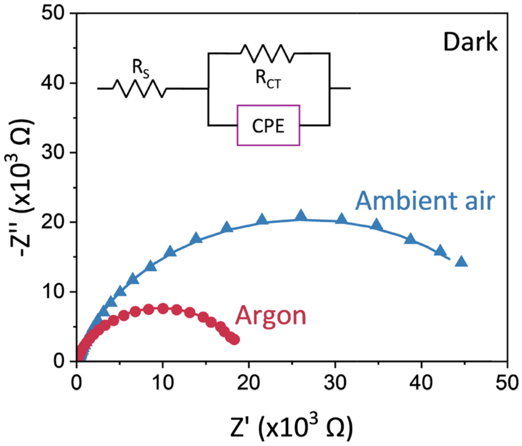

Fig. 7 EIS spectra of BFO thin films annealed in ambient air and argon measured in the dark. Inset shows the equivalence circuit used to fit the data.

hole recombination. In both these films, it is likely that interfacial electron transfer is in kinetic competition with electron–hole recombination at the surface. This notion can be confirmed by noticing an order increment in photocathodic current upon adding the electron acceptor to the solution that facilitates electron transfer (Fig. 1c and Fig. S1b). As per the proposed band bending model, the efficiency of electron transfer is favoured for BFO thin films annealed in argon (hence enhanced photocathodic current) compared to those annealed in ambient air.

To verify the band bending model proposed in Fig. 6, EIS measurements are conducted and presented in Fig. 7. The impedance in the charge transfer across the semiconductor–electrolyte interface is directly proportional to the radius of the semicircle. A smaller semicircle suggests a lower charge transfer resistance (consequently, higher charge-transfer efficiency) between the electrode/electrolyte interface.[43] Table S4 displays the fitting parameters of the obtained EIS plots. The relatively lower interfacial charge transfer resistance (R_{CT} = 1930 Ω) of argon annealed BFO, compared to ambient air annealed BFO (R_{CT} = 5300 Ω), agrees with the proposed band bending model discussed in Fig. 6.

3.4. Validating the effect of the Bi amount in BFO thin films on the PEC behaviour

As discussed earlier, due to its low melting point (hence volatile) and interaction with the annealing atmosphere, the escape of Bi from the lattice is promoted. As outlined in Fig. S7, the origin of annealing-atmosphere-dependent enhancement in PEC performance is ultimately due to the amount of Bi in the lattice (or Bi vacancies) and the resulting optoelectronic properties. To further confirm our hypothesis on the role of Bi, PEC activity was compared (Fig. S8) between stoichiometric and 20% Bi-excess BFO thin films, both annealed in ambient air. As expected, depending on the amount of Bi present in BFO, 20% Bi-excess BFO showed almost two times higher photocathodic current density than its stoichiometric counterpart. This finding further corroborates the crucial effect of Bi amount in BFO on the photocathodic behaviour.

The work presented here emphasises the effect of the often-ignored annealing atmosphere on the interplay between defect chemistry and optoelectronic properties. The work presented here provides comprehensive insight into the origin of the annealing-atmosphere-dependent PEC activity of the BFO thin films. It is emphasized that the role of defects will not just influence PEC activity, but various applications of BFO in ferroelectric behaviour, sensing, and less explored piezocatalysis.

4. Conclusion

Unlike the usually employed doping or post-synthesis approaches, which are not specific and are thus intricate to tune defects of interest, this work revealed how changing the annealing atmosphere can favourably be used as a facile approach for controlling the optoelectronic properties of BFO thin films. The origin of approximately four times enhancement in the photocathodic current for BFO just by changing the annealing atmosphere from ambient air to argon was attributed to a range of optoelectronic properties (defect chemistry, carrier concentration, band bending, and charge transfer) that originated from Bi vacancy creation. Besides its volatile nature owing to its low melting point, the extent of Bi interaction with the gas in the annealing atmosphere played a crucial role in governing the overall stoichiometry and the resulting defects. This work offered mechanistic insights into the formation of vacancies and systematically unravelled the often-ignored role of the annealing atmosphere in the defect formation and PEC performance of BFO thin films. The results provide an alternate and straightforward approach to rationally control the defects to enhance the function and applications of BFO in piezocatalysis, sensing, ferroelectricity and other emerging applications.

Author contributions

S. R. K. conducted the synthesis, structural/surface/optoelectronic characterization of the materials, and photoelectrochemical study. S. R. K. and D. H. K. M. wrote the first version of the article. S. N. V. conducted leakage current measurements supervised by N. K. K. The article was written through contributions from all authors.

Conflicts of interest

The authors declare no conflict of interest.

Data availability

The data supporting this article have been included as part of the manuscript and the supplementary information (SI). Supplementary information: Detailed stream tables and additional data relevant to the XPS and XRD analyses and PEC water splitting data. See DOI: **https://doi.org/10.1039/d5ma00995b**.

Acknowledgements

D. H. K. M. acknowledges funding from the Technology Mission Division (Energy, Water & all Others), Department of Science & Technology, Ministry of Science & Technology, Government of India, Reference Number DST/TMD/IC-MAP/2K20/02, the project titled ''Integrated Clean-Energy Material Acceleration Platform (IC-MAP) on bioenergy and hydrogen''. S. R. K. acknowledges the INSPIRE (IF240089) fellowship from the Department of Science & Technology, Government of India.

References

1 X. Yang and D. Wang, Photocatalysis: From Fundamental Principles to Materials and Applications, *ACS Appl. Energy Mater.*, 2018, **1**(12), 6657–6693, DOI: **10.1021/acsaem.8b01345**.

2 C. Avcıoğlu, S. Avcıoğlu, M. F. Bekheet and A. Gurlo, Photocatalytic Overall Water Splitting by SrTiO3: Progress Report and Design Strategies, *ACS Appl. Energy Mater.*, 2023, **6**(3), 1134–1154, DOI: **10.1021/acsaem.2c03280**.

3 H. Nishiyama, T. Yamada and M. Nakabayashi, *et al.*, Photocatalytic solar hydrogen production from water on a 100-m^2 scale, *Nature*, 2021, **598**(7880), 304–307, DOI: **10.1038/s41586-021-03907-3**.

4 F. Bhom and Y. M. Isa, Photocatalytic Hydrogen Production Using TiO2 -based Catalysts: A Review, *Global Challenges*, 2024, **8**(11), 2400134, DOI: **10.1002/gch2.202400134**.

5 G. Fang, Z. Liu and C. Han, *et al.*, CoNiO2 as a novel water oxidation cocatalyst to enhance PEC water splitting performance of BiVO4, *Chem. Commun.*, 2020, **56**(64), 9158–9161, DOI: **10.1039/D0CC03516E**.

6 S. Gulati, K. Goyal, A. Arora, S. Kumar, M. Trivedi and S. Jain, Bismuth ferrite (BiFeO3) perovskite-based advanced nanomaterials with state-of-the-art photocatalytic performance in water clean-up, *Environ. Sci.*, 2022, **8**, 1590–1618, DOI: **10.1039/D2EW00027J**.

7 X. Li, Z. Wang and W. Ji, *et al.*, Polarization Alignment in Polycrystalline BiFeO3 Photoelectrodes for Tunable Band Bending, *ACS Nano*, 2023, **17**(22), 22944–22951, DOI: **10.1021/acsnano.3c08081**.

8 M. Gunawan, O. Bowdler and S. Zhou, *et al.*, Ferroelectric Polarization-Induced Performance Enhancements in BiFeO3/BiVO4 Photoanodes for Photoelectrochemical Water Splitting, *Adv. Funct. Mater.*, 2025, **35**, 2417651, DOI: **10.1002/adfm.202417651**.

9 C. Murugan, A. S. Mary and A. Pandikumar, Fabrication and Performance Validation of BiVO4 Photoanode-Based Prototype Photoelectrochemical Cells with Different Sizes and Reducing the Photocurrent Density Loss with Different Conductive Patterns, *Ind. Eng. Chem. Res.*, 2024, **63**(10), 4329–4337, DOI: **10.1021/acs.iecr.3c04013**.

10 J. Li, L. Guo, N. Lei, Q. Song and Z. Liang, Metallic Bi Nanocrystal-Modified Defective BiVO4 Photoanodes with Exposed (040) Facets for Photoelectrochemical Water Splitting, *ChemElectroChem*, 2017, **4**(11), 2852–2861, DOI: **10.1002/celc.201700680**.

11 P. P. Kunturu, S. Bera, H. Johnson and M. N. Tsampas, Scaled-Up Zero-Gap Photoelectrochemical Device Based on Abundant Materials for Bias-Free Solar Hydrogen Production, *Artif. Photosynth.*, 2025, **1**(2), 106–116, DOI: **10.1021/aps.4c00023**.

12 E. N. Fernandez, R. van de Krol and F. F. Abdi, Tuning the Optical and Photoelectrochemical Properties of Epitaxial BiVO4 by Lattice Strain, *Small Struct.*, 2024, **5**(9), 2400097, DOI: **10.1002/sstr.202400097**.

13 Y. Li, L. Lin and F. Wu, *et al.*, In situ modification of bismuth oxyhalide photocatalysts with natural chlorophyll for enhanced photocatalytic performance, *RSC Adv.*, 2025, **15**(7), 4820–4828, DOI: **10.1039/D5RA00008D**.

14 G. Fang, Z. Liu and C. Han, Enhancing the PEC water splitting performance of BiVO4 co-modifying with NiFeOOH and Co-Pi double layer cocatalysts, *Appl. Surf. Sci.*, 2020, **515**, 146095, DOI: **10.1016/j.apsusc.2020.146095**.

15 S. Vidhya, Y. Subramanian and K. Durgadevi, *et al.*, Synthesis and characterization of a heterogeneous ternary nanocomposite photocatalyst BiFeO3-Graphene-NaNbO3 for the degradation of MB dye disrupting pulmonary organs, *Opt. Laser Technol.*, 2025, **181**, 111798, DOI: **10.1016/j.optlastec.2024.111798**.

16 L. Smith, J. Shield, Z. Ahmadi, S. Jeelani and V. Rangari, Synthesis and characterization of bismuth ferrite particles using a nano-agitator bead mill, *AIP Adv.*, 2023, **13**(3), 035004, DOI: **10.1063/5.0132099**.

17 N. V. Srihari, S. Bayari, S. Kumar, M. Padaki and K. K. Nagaraja, Comprehensive investigation into the influence of oxygen vacancies on the ferroelectric properties of spin coated bismuth ferrite thin films, *Phys. Scr.*, 2024, **99**(7), 075917, DOI: **10.1088/1402-4896/ad4fec**.

18 N. P. Prasad, M. Rohnke and M. A. Verheijen, *et al.*, Role of Excess Bi on the Properties and Performance of BiFeO3 Thin-Film Photocathodes, *ACS Appl. Energy Mater.*, 2023, **6**(24), 12237–12248, DOI: **10.1021/acsaem.3c01926**.

19 J. Wu, J. Wang, D. Xiao and J. Zhu, Valence-driven electrical behavior of manganese-modified bismuth ferrite thin films, *J. Appl. Phys.*, 2011, **109**(12), 124118, DOI: **10.1063/1.3596826**.

20 D. You, L. Liu and Z. Yang, *et al.*, Polarization-induced internal electric field to manipulate piezo-photocatalytic and ferro-photoelectrochemical performance in bismuth ferrite nanofibers, *Nano Energy*, 2022, **93**, 106852, DOI: **10.1016/j.nanoen.2021.106852**.

21 S. Man, X. Leng and J. Bai, *et al.*, Enhancement of photoelectrochemical performance of BiFeO3 by Sm3+ doping, *Ceram. Int.*, 2023, **49**(7), 10255–10264, DOI: **10.1016/j.ceramint.2022.11.205**.

22 A. K. Vishwakarma, M. Hussain, S. K. Verma, V. Shukla, M. A. Shaz and O. N. Srivastava, Synthesis and characterizations of graphene/Sm doped BiFeO3 composites photoanode

for efficient photo-electrochemical water splitting, *Int. J. Hydrogen Energy*, 2021, **46**(29), 15550–15560, DOI: **10.1016/j.ijhydene.2021.02.115**.

23 Y. Wang, M. Zhang and Y. Yue, *et al.*, Chemical Solution Deposition of Single-Phase BiFeO3 Thin Films on Transparent Substrates, *Solar RRL*, 2022, **6**(7), 2200124, DOI: **10.1002/solr.202200124**.

24 A. Z. Simões, C. S. Riccardi, M. L. Dos Santos, F. G. Garcia, E. Longo and J. A. Varela, Effect of annealing atmosphere on phase formation and electrical characteristics of bismuth ferrite thin films, *Mater. Res. Bull.*, 2009, **44**(8), 1747–1752, DOI: **10.1016/j.materresbull.2009.03.011**.

25 Y. Sun, W. Cai and R. Gao, *et al.*, Effects of annealing atmosphere on microstructure, electrical properties and domain structure of BiFeO3 thin films, *J. Mater. Sci.: Mater. Electron.*, 2017, **28**(16), 12039–12047, DOI: **10.1007/s10854-017-7015-2**.

26 A. Valipour, N. Hamnabard, S. M. H. Meshkati, M. Pakan and Y. H. Ahn, Effectiveness of phase- and morphology-controlled MnO2 nanomaterials derived from flower-like δ-MnO2 as alternative cathode catalyst in microbial fuel cells, *Dalton Trans.*, 2019, **48**(16), 5429–5443, DOI: **10.1039/C9DT00520J**.

27 S. Khatun and P. Roy, Valence State Regulated Nickel Iron Layered Double Hydroxides by Amine Intercalation as Efficient Electrocatalysts for Seawater Oxidation, *ACS Appl. Energy Mater.*, 2024, **7**(20), 9110–9120, DOI: **10.1021/acsaem.4c00979**.

28 S. Chandrappa, S. J. Galbao, A. Furube and D. H. K. Murthy, Extending the Optical Absorption Limit of Graphitic Carbon Nitride Photocatalysts: A Review, *ACS Appl Nano Mater.*, 2023, **6**(21), 19551–19572, DOI: **10.1021/acsanm.3c04740**.

29 Y. Wang, D. Chen and S. Wang, *et al.*, Photoassisted Electrodeposition of Cobalt-Phosphate Cocatalyst on BiFeO3 Thin Film Photoanode for Highly Efficient Photoelectrochemical Performances of Water Oxidation, *J. Electrochem. Soc.*, 2019, **166**(8), D308–D314, DOI: **10.1149/2.0711908jes**.

30 H. Wang, Y. Zheng, M. Q. Cai, H. Huang and H. L. W. Chan, First-principles study on the electronic and optical properties of BiFeO3, *Solid State Commun.*, 2009, **149**(15–16), 641–644, DOI: **10.1016/j.ssc.2009.01.023**.

31 S. Chandrappa, P. S. Sankara Rama Krishnan and S. Nagaraju Myakala, *et al.*, Oxygen Vacancies and Ti3+ In-Gap Defects Dictate Photocatalytic H2 Generation in BaTiO3, *ACS Appl. Energy Mater.*, 2024, **7**(23), 11076–11085, DOI: **10.1021/acsaem.4c02142**.

32 J. F. Moulder, W. F. Stickle, P. E. Sobol, K. D. Bomben and J. Chastain, *Handbook of X-Ray Photoelectron Spectroscopy A Reference Book of Standard Spectra for Identification and Interpretation of XPS Data*, 1992.

33 T. Yang, J. Wei, Y. Guo, Z. Lv, Z. Xu and Z. Cheng, Manipulation of Oxygen Vacancy for High Photovoltaic Output in Bismuth Ferrite Films, *ACS Appl. Mater. Interfaces*, 2019, **11**(26), 23372–23381, DOI: **10.1021/acsami.9b06704**.

34 H. Zhang, M. C. Nagashree and R. F. Webster, *et al.*, Optical Control of Ferroelectric Imprint in BiFeO3, *Adv. Funct. Mater.*, 2025, **35**(31), 2502700, DOI: **10.1002/adfm.202502700**.

35 S. Kumari, K. Anand and M. Alam, *et al.*, Enhancement of Multiferroic and Optical Properties in BiFeO3 Due to Different Exchange Interactions Between Transition and Rare Earth Ions, *Phys. Status Solidi B*, 2023, **260**(9), 2300026, DOI: **10.1002/pssb.202300026**.

36 W. A. Wani, H. Venkataraman and K. Ramaswamy, Exploring current conduction dynamics in multiferroic BiFeO3 thin films prepared via modified chemical solution method, *Sci. Rep.*, 2024, **14**(1), 25578, DOI: **10.1038/s41598-024-76458-y**.

37 *Biological Chemistry of Arsenic, Antimony and Bismuth*, ed. Sun H., Wiley, 2010, DOI: **10.1002/9780470975503**.

38 Z. Zhang, P. Wu, L. Chen and J. Wang, Density functional theory plus U study of vacancy formations in bismuth ferrite, *Appl. Phys. Lett.*, 2010, **96**(23), 232906, DOI: **10.1063/1.3447369**.

39 Q. Xu, M. Sobhan, Q. Yang, F. Anariba, K. Phuong Ong and P. Wu, The role of Bi vacancies in the electrical conduction of BiFeO3: a first-principles approach, *Dalton Trans.*, 2014, **43**(28), 10787–10793, DOI: **10.1039/C4DT00468J**.

40 S. Chandrappa, S. J. Galbao and P. S. Sankara Rama Krishnan, *et al.*, Iridium-Doping as a Strategy to Realize Visible-Light Absorption and p-Type Behavior in BaTiO3, *J. Phys. Chem. C*, 2023, **127**(25), 12383–12393, DOI: **10.1021/acs.jpcc.3c02942**.

41 J. Bisquert, P. Cendula, L. Bertoluzzi and S. Gimenez, Energy Diagram of Semiconductor/Electrolyte Junctions, *J. Phys. Chem. Lett.*, 2014, **5**(1), 205–207, DOI: **10.1021/jz402703d**.

42 A. J. Bard and L. R. Faulkner, *Electrochemical Methods: Fundamentals and Applications*, John Wiley & Sons, Inc., 2001.

43 A. C. Lazanas and M. I. Prodromidis, Electrochemical Impedance Spectroscopy–A Tutorial, *ACS Meas. Sci. Au*, 2023, **3**(3), 162–193, DOI: **10.1021/acsmeasuresciau.2c00070**.